www.sciencemag.org/cgi/content/full/336/6077/69/DC1

Supplementary Materials for

The Role and Implications of Bassanite as a Stable Precursor Phase to Gypsum Precipitation

A. E. S. Van Driessche, L. G. Benning,* J. D. Rodriguez-Blanco, M. Ossorio, P. Bots, J. M. García-Ruiz*

*To whom correspondence should be addressed. E-mail: l.g.benning@leeds.ac.uk (L.G.B.); jmgruiz@ugr.es (J.M.G.-R.)

Published 6 April 2012, *Science* **336**, 69 (2012)
DOI: 10.1126/science.1215648

This PDF file includes:

Materials and Methods

Ambient sample preparation

Solids were obtained at 21 ºC by adding a $CaCl_2 \cdot 2H_2O$ solution to a Na_2SO_4 (Analytical grade, Sigma) solution under continuous stirring. In all cases equimolar and equivolumetric solutions were mixed to obtain final calcium sulfate concentrations of 25 to 150 mM. At selected time steps (between 10 seconds and 20 minutes), 20 µL aliquots were rapidly vacuum/solvent (ethanol) filtered (*9*) directly onto carbon coated Cu-TEM grids for subsequent imaging. This sample preparation mode is referred to as 'vacuum/solvent-filtered' (V/SF). In order to demonstrate that this sample preparation mode does not affect the precipitation path, larger amounts of precipitates were prepared for powder X-ray diffraction (XRD) analyses using bigger solution volumes and vacuum filtering the samples in three modes: (i) vacuum filtering the original solution with water only, (ii) vacuum filtering the original solution with ethanol as the solvent, and (iii) vacuum filtering the solution with isopropanol as the solvent (Fig. S1).

Cryogenic sample preparation

A series of samples were prepared using an ultra-rapid cryo-quench freezing Vitrobot system (Vitrobot Mark V, FEI companyTM). This way possible sample preparation and handling artifacts due to drying or due to solvent interactions in the above described vacuum/solvent filtration were avoided because reacting solution droplets were instantaneously flash-frozen onto TEM grids (*10*). Using the 75 mM calcium sulfate solutions, samples were prepared at times intervals between 1 and 6 minutes. Small aliquots (3 µl) of solution were deposited on TEM grids, which were flash-frozen in liquid ethane (*27*) using the standard guillotine plunging mode of the Vitrobot, thus instantaneously quenching the reaction and vitrifying the samples. The frozen TEM grids were re-equilibrated in a liquid nitrogen dewar after which they were transferred to a vacuum desiccator where the vitrified ice was slowly (over ~ 12 h) sublimated prior to imaging. This sample preparation mode is hereafter referred to as cryo-quenching (C-Q).

Powder X-ray diffraction (XRD)

Powder patterns were acquired using a PANalytical diffractometer (X'Pert Pro) with Bragg-Brentano configuration, PIXcel multichannel detector, and programmable divergence slits, with a Cu anode, Kα1 and Kα2 wavelengths. Patterns were collected from 5 to 80º (2θ) and analyzed with the "X-Powder" software, using the ICDD-PDF2 database (*28*). Although gypsum was found in all patterns, bassanite Bragg peaks were unambiguously identified at all experimental conditions (i.e., in all cases undersaturated with respect to bassanite) but also regardless of the vacuum/solvent filtration approach (Fig. S1 and insets).

High-resolution microspectroscopic analyses

The multi-stage structural development (nature, morphology and size) of the solid reaction products were characterized by high-resolution transmission electron microscopy (HR-TEM) using a FEI Tecnai F20 field emission gun microscope fitted with a HAADF detector and a 80 mm X-Max SDD detector and a Gatan Orius SC600A CCD camera

(also used for selected area electron diffraction, SAED, patterns). Solid samples were collected directly on TEM grids at various time steps (10 seconds – 20 minutes) either through vacuum/solvent filtration or through cryo-quenching. As explained in the main text, the bassanite nanorods showed a porous aspect (main text Fig. 1c and 1d, and SOM Fig. S2b) that has not been observed in the first stage bassanite nanoparticles, regardless if images were collected from the ambient temperature vacuum/solvent filtered samples or the cryo-quenched TEM grids. To demonstrate that these were not a consequence of the HR-TEM imaging (i.e., not beam damage) repeated low dose imaging of the same nanorods through tilt series with a 5 º angle step over a 90 º range was carried out. The resulting tilt series demonstrated the persistence and unchanging nature of these pores, thus excluding beam damage induced porosity. It is worth noting, that during all TEM imaging and analyses the microscope was operated in a low dose mode in order to avoid any beam damage on the observed particles. Although, we cannot rule out that the porosity in the nanorods may have been induced during introduction of the samples into the TEM vacuum, we would have expected that if the observed porosity is a consequence of the TEM vacuum that this same effect should produce similar consequences at the bassanite nanoparticles – yet in none of the >80 analyzed bassanite nanoparticles has this been seen.

Turbidity measurements

In order to monitor the concentration dependent precipitation induction times, the development of turbidity in the reacting solutions was monitored by *in situ* and time resolved (1 sec/pattern) UV-VIS (Uvikon XL spectrophotometer) with measurements carried out at 580 nm. Experiments at the conditions described above were performed in a cuvette inside a stirred module with spectra recorded every second up to 13 hours. The resulting supersaturation dependent turbidity curves (Fig. S2a) show that with an increase in the SI the induction time decreased dramatically. All experiments were repeated 3-5 times and although small differences in onset and slope of the resulting curves were observed, the overall changes in transmission with time and the trend of increasing induction time with decreasing concentration were identical in all cases. For experiments with concentrations ≥50 mM, the solutions became turbid and then opaque within the first 4 minutes of reaction. They reached the plateau within 25 seconds (150 mM) and respectively ~1 hour (50 mM) and all >50 mM reactions produced bassanite and ultimately gypsum. However, at 25 mM, even after 13 hours no visible turbidity developed, yet when the solution was vacuum/solvent filtered and imaged bassanite nanoparticles were observed (Fig. S2b).

Gypsum and Bassanite stability data

Experiments were performed above and below the bulk solubility of bassanite (SI_{Bas} = -0.72 to +0.18) but supersaturated with respect to gypsum (SI_{Gyp} = +0.14 to +1.04). The solubility products (K) and the saturation indexes (SI) were calculated with PHREEQC using the LLNL database (2*9*). In Fig. S3 all available literature data for the experimentally determined solubilities for both gypsum and bassanite are plotted [Freyer and Voigt and refs. therein, (*13*)] and compared with the solubility curves calculated with PHREEQC. The calculated solubility curve shows a good fit to the experimentally determined gypsum solubility data, whereas the calculated solubility curve for bassanite

only matches a subset of the experimentally determined data. The data in the LLNL database, from which the plotted bassanite curve was calculated, relies on a self-consistent algorithm with the bassanite and gypsum data from the National Bureau of Standards tables as compiled by Wagman and coworkers (*12*). However, only bulk bassanite solubility data is available in the literature (*13* and refs. therein) and most of that data was not derived from equilibrium solubility measurements but represents ion concentrations from the dissolution of bassanite, analyzed just before the solutions reached concentrations where gypsum precipitated, since below 100 ºC a solution saturated with respect to bassanite is always also saturated with respect to gypsum (*30*). Hence, the real solubility, even of bulk bassanite is still problematic and highly debated (*13*, *30*).

Supplementary Text

Thermodynamic considerations

Although one crystalline polymorph is thermodynamically the most stable under a given set of conditions, others are often only slightly less stable (or metastable) by a few kilojoules per mole (e.g. *18*, *21*). It has furthermore been demonstrated for several systems (*21* and references therein) that the order of thermodynamic stability can be inverted by for example changes in the crystal size. To evaluate this for the calcium sulfate system, we initially determined the transformation enthalpy between bassanite and gypsum with the heats of reaction calculated from the standard formation enthalpies (1 bar, 25 °C):

$CaSO_4.0.5H_2O_{(s)} \rightarrow Ca^{2+}_{(aq)} + SO_4^{2-}_{(aq)} + 0.5H_2O_{(l)}$ Δ_rH°=-18 kJ/mol

$Ca^{2+}_{(aq)} + SO_4^{2-}_{(aq)} + 2H_2O_{(l)} \rightarrow CaSO_4.2H_2O_{(s)}$ Δ_rH°= 1 kJ/mol

---

$CaSO_4.0.5H_2O_{(s)} + 3/2H_2O_{(l)} \rightarrow CaSO_4.2H_2O_{(s)}$ ΔrH°= -17 kJ/mol

Thus a change in Δ_rH° of ~17 kJ/mol in the solution enthalpy is necessary to explain the appearance of bassanite, if the Δ_rH° for the bulk phases are identical to the Δ_rH° for the nanoparticulate phases. This value is at the higher end of the Δ_rH° compared to the systems discussed in the work of Navrotsky (*21*). We assume that at ambient conditions the surface free energies are comparable to the surface enthalpies because the surface entropy is suggested to be negligible compared to the surface enthalpy (*21*). When the Δ_rH° for bulk bassanite and gypsum are combined with the experimentally obtained values for the surface free energies of gypsum [~40 mJ/m^2, (*31-34*)] and bassanite [~9 mJ/m^2, (*35*)] the relation between surface area and Δ_rH° for nanoparticles can be obtained using (*18*):

$$\Delta_rH^\circ (\text{nano}) = \Delta_rH^\circ(\text{bulk}) + A\gamma \quad \text{(S1)}$$

where, A represents the surface area in m^2/mol and γ represents the surface energy in kJ/mol and the resulting values are plotted in Fig. 3c in the main text. Although this relation explains why nanoparticulate bassanite can form prior to gypsum, it does not explain the occurrence of bassanite nanoparticles far below their bulk solubility. Additionally, the surface area at which the Δ_rH° for bassanite is lower than that of gypsum becomes unrealistically high (i.e. >500000 m^2/mol).

However, the surface energy does not have to be a constant, specifically because with decreasing particle size the surface of nanoparticles will contain the largest proportion of the reactive sites and the surface and interior of a nanoparticle become almost indistinguishable. Zhang and coworkers (*23* and refs. therein) proposed that with a decrease in particle size (and, thus, an increase in surface area) the surface energy of crystalline nanoparticles approaches zero. This concept was applied in the current study to estimate the $\Delta_r H^\circ$ as a function of surface area (main text Fig. 3c). This approach leads to a lower surface area at which bassanite becomes more stable than gypsum. However, because $A\gamma$ decreases to 0 and,

$$\Delta_r H^\circ \text{ (nano)} = \Delta_r H^\circ \text{ (bulk)}, \quad \text{(S2)}$$

at the smallest particle size this model does not account for the formation of bassanite nanoparticles below its bulk solubility. Another study, on the formation of ZnS nanosheets (*22*), also proposed that the surface energy is variable and depends on particle size as follows:

$$\gamma = \gamma^{bulk} + b/\delta \quad \text{(S3)}$$

Here γ^{bulk} is the surface energy for the bulk phase, δ is the thickness of the nanosheet (inversely proportional to the surface area), and b is a constant, which represents a destabilizing physical interaction (*22*). Rearranging Eq. S3 so that it does not apply to a nanosheet, but that it can calculate the surface energy of a nanoparticle gives:

$$A \propto M/(\rho \cdot \delta) \quad \text{(S4)}$$

where ρ is the density of the phase and M the molecular weight, and thus:

$$\gamma = \gamma^{bulk} + b \cdot A \cdot (\rho/M) \quad \text{(S5)}$$

If we use the relation described in Eq. S5, and assume an effective negative surface energy for bulk bassanite, which increases with surface area [i.e. b >0, (*22*)], the $\Delta_r H^\circ$ for bassanite becomes lower than the $\Delta_r H^\circ$ for gypsum and this happens at a significantly lower surface area range (Fig. 3c). Taken together, this last model leads to a decrease in the $\Delta_r H^\circ$ for bassanite with increasing surface area, providing an explanation for the formation of bassanite nanoparticles and nanorods far below its bulk solubility (Fig. 3c).

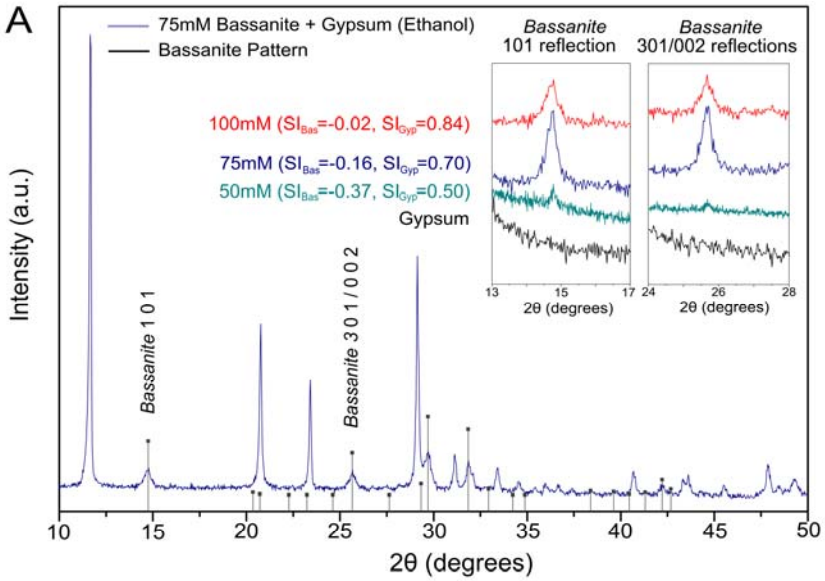

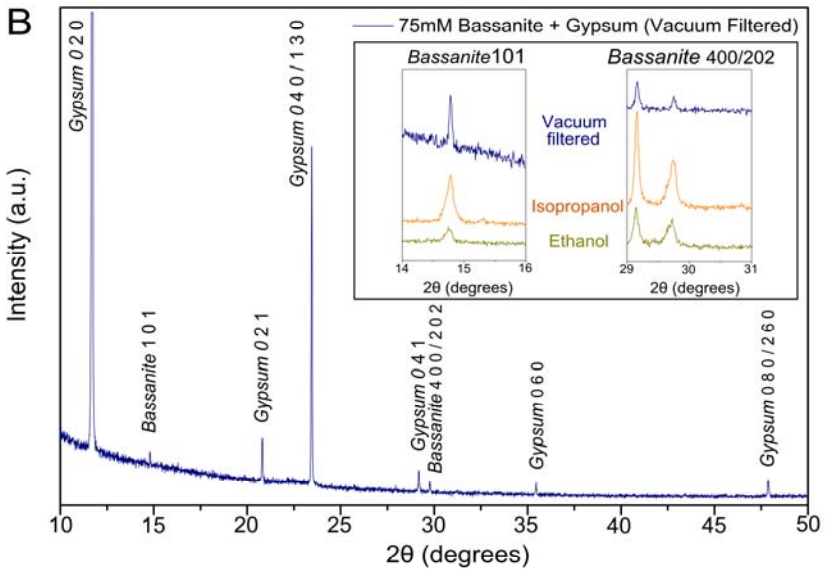

Phases	h k l	d-spacing (Å)	2θ *CuKa* (deg)	Intensity (%)
Bassanite (PDF2 33-310)	1 0 1	6.0000	14.752	70.0
	3 0 1/0 0 2	3.4690	25.659	55.0
	4 0 0/2 0 2	3.0060	29.696	100.0
Gypsum (PDF2 33-311)	0 2 0	7.6300	11.580	42.3
	0 2 1	4.2800	20.730	88.1
	0 4 0/1 3 0	3.8000	23.400	22.7
	0 4 1	3.0650	29.111	75.0
	-1 1 2	2.7890	32.066	23.9

Fig. S1.

(a) XRD patterns of samples from 50 mM (green), 75 mM (blue, inset and main) and 100 mM (red) calcium sulfate solutions quenched after 20, 3 and 2 min, showing bassanite Bragg peaks at all conditions, compared with a pure gypsum pattern (black). (b) XRD patterns of vacuum-filtered (blue), vacuum/ethanol filtered (light green) and vacuum/isopropanol filtered (red) samples, all showing bassanite Bragg peaks. Below the figures shown is a table with relevant bassanite and gypsum XRD data.

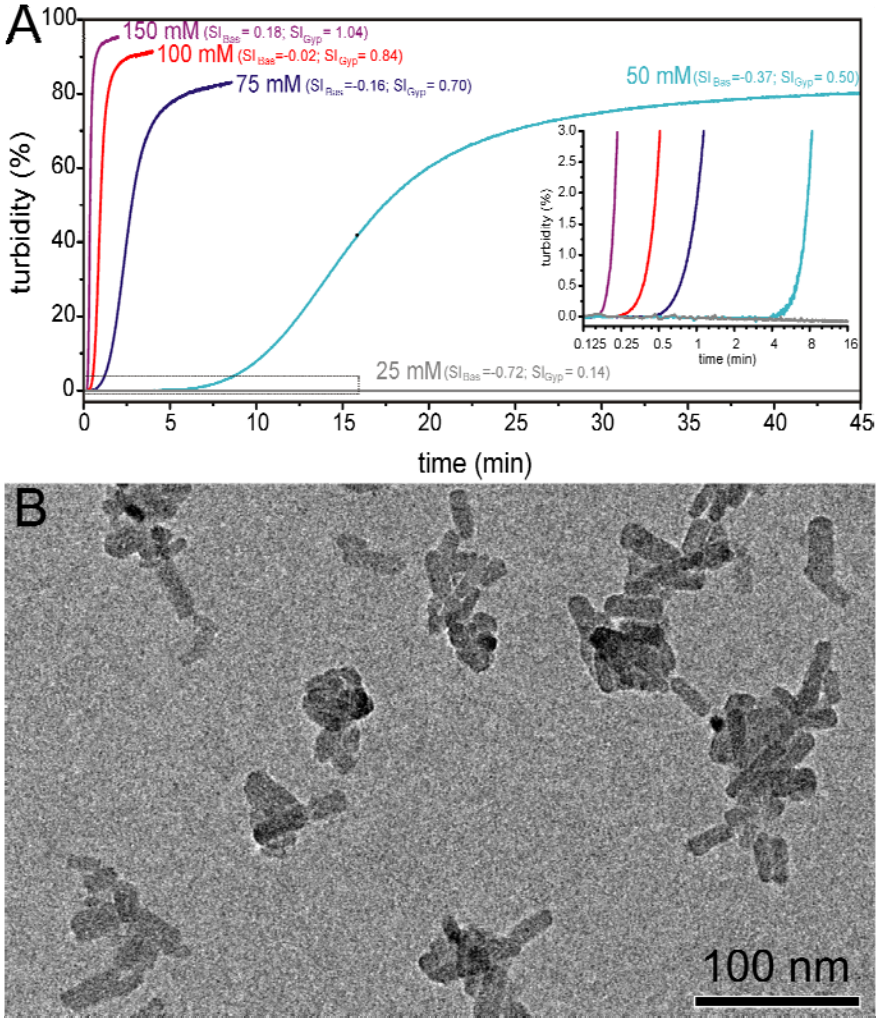

Fig. S2

(a) Turbidity curves for experiments at the concentrations indicated, together with the calculated saturation indexes for bassanite (SI_{Bas}) and gypsum (SI_{Gyp}). The inset shows the onset of precipitation on a log time scale. (b) HR-TEM image of small and poorly developed bassanite nanorods from the experiment at the lowest supersaturation (SI_{Bas} = -0.72 and SI_{Gyp}=+0.14), where even after 13 hours no visible turbidity was observed in the solution [see (a)], and even after 24 hours no gypsum formed.

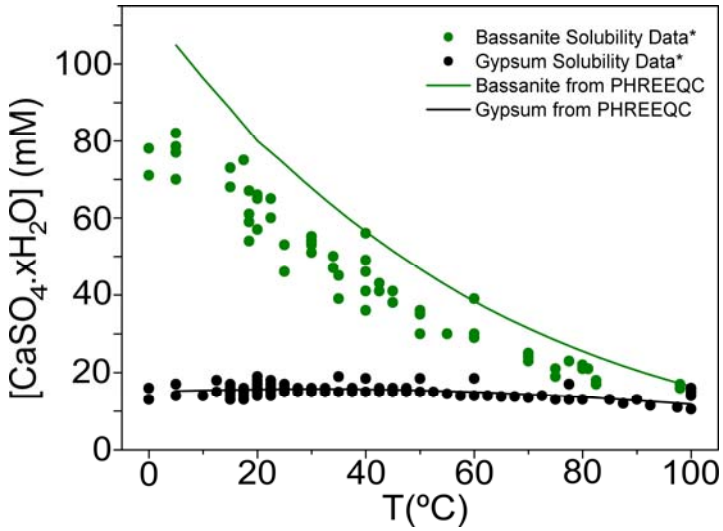

Fig. S3

Solubility data for gypsum and bassanite as a function of temperature. Symbols are experimental data (* from *13* and refs. therein) and lines were calculated with PHREEQC using the LLNL database (*30*).

References

1. R. Buick, J. S. R. Dunlop, Evaporitic sediments of Early Archaean age from the Warrawoona Group, North Pole, Western Australia. *Sedimentology* **37**, 247 (1990).

2. J. K. Warren, *Evaporites: Sediments, Resources and Hydrocarbons* (Springer-Verlag, Berlin, 2006).

3. Y. Langevin, F. Poulet, J. P. Bibring, B. Gondet, Sulfates in the north polar region of Mars detected by OMEGA/Mars Express. *Science* **307**, 1584 (2005).

4. J. J. Wray *et al*., Identification of the Ca-sulfate bassanite in Mawrth Vallis, Mars. *Icarus* **209**, 416 (2010).

5. S. B. Ahmed, M. Tlili, M. B. Amor, H. B. Bacha, B. Elleuch, Calcium sulphate scale prevention in a desalination unit using the SMCEC technique. *Desalination* **167**, 311 (2004).

6. B. Mi, M. Elimelech, Gypsum scaling and cleaning in forward osmosis: Measurements and mechanisms. *Environ. Sci. Technol.* **44**, 2022 (2010).

7. N. B. Singh, B. Middendorf, Calcium sulphate hemihydrate hydration leading to gypsum crystallization. *Prog. Cryst. Growth Charact. Mater.* **53**, 57 (2007).

8. Y. W. Wang, Y. Y. Kim, H. K. Christenson, F. C. Meldrum, A new precipitation pathway for calcium sulfate dihydrate (gypsum) via amorphous and hemihydrate intermediates. *Chem. Commun.* **48**, 504 (2012).

9. J. D. Rodríguez-Blanco, S. Shaw, L. G. Benning, The kinetics and mechanisms of amorphous calcium carbonate (ACC) crystallization to calcite, via vaterite. *Nanoscale* **3**, 265 (2011).

10. D. J. Tobler, S. Shaw, L. G. Benning, Quantification of initial steps of nucleation and growth of silica nanoparticles: An in-situ SAXS and DLS study. *Geochim. Cosmochim. Acta* **73**, 5377 (2009).

11. See supplementary materials on *Science* Online.

12. D. D. Wagman *et al*., *J. Phys. Chem. Ref. Data* **11**, suppl. 2 (1982).

13. D. Freyer, W. Voigt, Crystallization and phase stability of $CaSO_4$ and $CaSO_4$-based salts. *Monatsh. Chem.* **134**, 693 (2003).

14. M. C. Ball, L. S. Norwood, Studies in the system $CaSO_4 + H_2O$. Part 6. Surface chemistry and porosity of the $CaSO_4$ hemihydrates. *J. Chem. Soc. Faraday Trans. I* **74**, 1477 (1978).

15. L. Brečević, A. E. Nielsen, Solubility of amorphous calcium carbonate. *J. Cryst. Growth* **98**, 504 (1989).

16. L. B. Gower, Biomimetic model systems for investigating the amorphous precursor pathway and its role in biomineralization. *Chem. Rev.* **108**, 4551 (2008).

17. A. Dey *et al*., The role of prenucleation clusters in surface-induced calcium phosphate crystallization. *Nat. Mater.* **9**, 1010 (2010).

18. J. M. McHale, A. Auroux, A. J. Perrotta, A. Navrotsky, Surface energies and thermodynamic phase stability in nanocrystalline aluminas. *Science* **277**, 788 (1997).

19. M. R. Ranade *et al*., Energetics of nanocrystalline TiO_2. *Proc. Natl. Acad. Sci. U.S.A.* **99** (suppl. 2), 6476 (2002).

20. A. Navrotsky, *Rev. Mineral.* **29**, 309 (1994).

21. A. Navrotsky, Energetic clues to pathways to biomineralization: Precursors, clusters, and nanoparticles. *Proc. Natl. Acad. Sci. U.S.A.* **101**, 12096 (2004).

22. Z. Lin, B. Gilbert, Q. Liu, G. Ren, F. Huang, A thermodynamically stable nanophase material. *J. Am. Chem. Soc.* **128**, 6126 (2006).

23. H. Zhang, B. Chen, J. F. Banfield, The size dependence of the surface free energy of titania nanocrystals. *Phys. Chem. Chem. Phys.* **11**, 2553 (2009).

24. B. Winkler, B. Hennion, Low temperature dynamics of molecular H_2O in bassanite, gypsum and cordierite investigated by high resolution incoherent inelastic neutron scattering. *Phys. Chem. Miner.* **21**, 539 (1994).

25. J. M. García-Ruiz, R. Villasuso, C. Ayora, A. Canals, F. Otálora, Formation of natural gypsum megacrystals in Naica, Mexico. *Geology* **35**, 327 (2007).

26. A. E. S. Van Driessche, J. M. García-Ruíz, K. Tsukamoto, L. D. Patiño-Lopez, H. Satoh, Ultraslow growth rates of giant gypsum crystals. *Proc. Natl. Acad. Sci. U.S.A.* **108**, 15721 (2011).

27. S. U. Egelhaaf, P. Schurtenberger, M. Müller, New controlled environment vitrification system for cryo-transmission electron microscopy: Design and application to surfactant solutions. *J. Microsc.* **200**, 128 (2000).

28. J. D. Martin, *Using XPowder: A Software Package for Powder X-Ray Diffraction Analysis* (Granada, Spain, 2008).

29. D. L. Parkhurst, C. A. J. Appelo, *U.S. Geol. Surv. Water Resour. Invest. Rep. 99-4259* (1999).

30. L. Amathieu, R. Boistelle, Crystallization kinetics of gypsum from dense suspension of hemihydrate in water. *J. Cryst. Growth* **88**, 183 (1988).

31. S. He, J. E. Oddo, M. B. Tomson, The nucleation kinetics of calcium sulfate dihydrate in NaCl solutions up to 6 m and 90°C. *J. Colloid Interface Sci.* **162**, 297 (1994).

32. A. Lancia, D. Musmarra, M. Prisciandaro, Measuring induction period for calcium sulfate dihydrate precipitation. *AIChE J.* **45**, 390 (1999).

33. M. Prisciandaro, A. Lancia, D. Musmarra, Gypsum nucleation into sodium chloride solutions. *AIChE J.* **47**, 929 (2001).

34. M. Prisciandaro, A. Lancia, D. Musmarra, The retarding effect of citric acid on calcium sulfate nucleation kinetics. *Ind. Eng. Chem. Res.* **42**, 6647 (2003).

35. B. Guan, L. Yang, Z. Wu, Effect of Mg^{2+} ions on the nucleation kinetics of calcium sulfate in concentrated calcium chloride solutions. *Ind. Eng. Chem. Res.* **49**, 5569 (2010).